Journal of Alloys and Compounds 706 (2017) 584–588

Contents lists available at ScienceDirect

Journal of Alloys and Compounds

journal homepage: http://www.elsevier.com/locate/jalcom

Primary and secondary precipitates in a hierarchical-precipitate-strengthened ferritic alloy☆

Gian Song [a, *], Zhiqian Sun [a], Jonathan D. Poplawsky [b], Xiandong Xu [c], Mingwei Chen [c], Peter K. Liaw [a, **]

[a] Department of Materials Science and Engineering, The University of Tennessee, Knoxville, TN, 37996-2200, USA
[b] Center for Nano-phase Materials Sciences, Oak Ridge National Laboratory, Oak Ridge, TN, 37831, USA
[c] World Premier International Advanced Institute for Materials Research, Tohoku University, Sendai, 980-8577, Japan

ARTICLE INFO

Article history:
Received 24 November 2016
Received in revised form
17 January 2017
Accepted 26 February 2017
Available online 27 February 2017

Keywords:
Atom probe tomography
Ferritic steels
Heusler phases
Precipitation
Transmission electron microscopy (TEM)

ABSTRACT

The microstructures of a hierarchical-precipitate-strengthened ferritic alloy are characterized, using transmission-electron microscopy (TEM) and atom-probe tomography (APT). The alloy shows duplex precipitates. The primary precipitate with an average edge length of 90 nm consists of NiAl- and Ni_2TiAl-type phases, while the secondary precipitate with an average radius of 2 nm is a NiAl-type phase. Based on the APT results, the volume fractions of the primary and secondary precipitates were calculated, using the lever rule to be 17.3 and 2.3%, respectively.

1. Introduction

Ferritic steels have been widely employed for high-temperature applications, due to their low cost, high thermal conductivity, and low thermal expansion, as compared to austenitic steels [1–4]. High-Cr ferritic steels are strengthened by nano- and micro-scaled particles, have a small grain size, and contain a high density of dislocations [1,2,5,6]. However, the microstructural instability during the long-term exposure to elevated temperatures, characterized by the coarsening behavior of the precipitate/particle and grain size, as well as a reduction in the dislocation density, restricts their operating temperature to below 900 K [7–9]. There have been extensive efforts to develop creep-resistant ferritic steels with higher temperature capabilities, according to the current US project for the development of ultra-supercritical (USC) steam turbines [10–12], which requires an increase of the steam temperature to 1033 K and the steam pressure to 35 MPa [13].

Along the same lines, the NiAl-precipitate-strengthened ferritic alloys have received recent attention as candidate materials for numerous high-temperature applications, due to their promising creep properties and oxidation resistance [14–16]. Moreover, the structural similarity between the B2-NiAl precipitates and the body-centered-cubic (bcc) Fe matrix leads to the coarsening resistance of the NiAl precipitates during creep deformation [17,18]. However, as the temperature is increased to higher than 923 K, the NiAl-strengthened ferritic alloys exhibit the limited creep resistance, especially at high stresses [19]. The elevated-temperature deformation mechanisms of a NiAl-strengthened ferritic alloy have been investigated, using in-situ neutron-diffraction [20–22], the results of which suggest that the intense diffusion flow along the interfaces between the Fe matrix and NiAl precipitates plays a significant role in affecting the creep deformation [22].

☆ This manuscript has been authored by UT-Battelle, LLC under Contract No. DE-AC05-00OR22725 with the U.S. Department of Energy. The United States Government retains and the publisher, by accepting the article for publication, acknowledges that the United States Government retains a non-exclusive, paid-up, irrevocable, world-wide license to publish or reproduce the published form of this manuscript, or allow others to do so, for United States Government purposes. The Department of Energy will provide public access to these results of federally sponsored research in accordance with the DOE Public Access Plan (http://energy.gov/downloads/doe-public-access-plan).

* Corresponding author.
** Corresponding author.
E-mail addresses: gsong1@vols.utk.edu (G. Song), sunzhiqian2668@gmail.com (Z. Sun), poplawskyjd@ornl.gov (J.D. Poplawsky), xuxiandong000@gmail.com (X. Xu), mwchen@wpi-aimr.tohoku.ac.jp (M. Chen), pliaw@utk.edu (P.K. Liaw).

http://dx.doi.org/10.1016/j.jallcom.2017.02.271
0925-8388/

Recently, we have developed a new ferritic alloy consisting of $L2_1$-Ni_2TiAl precipitates reinforced by narrow B2-NiAl zones, which is referred to as the hierarchical-precipitate-strengthened ferritic alloy and is denoted as HPSFA in the present study [23]. The HPSFA was designed by adding the 2.2 atomic percent (at. %) Ti to a previously-studied NiAl-strengthened ferritic alloy (Fe-12.7Al-10.2Cr-9.0Ni-1.9Mo-0.14Zr-0.024B, at. %, denoted as FBB8 in the present study) [16]. This previous study revealed that the significant improvement in the creep resistance of HPSFA at 973 K was achieved by the presence of the hierarchical precipitates, which formed a coherent interface between the Fe matrix and precipitate phases with optimized elastic strains [23]. Fig. 1 shows the Larson–Miller parameter (LMP) of HPSFA [23], and is compared with FBB8 [24] and conventional steels [P92; Fe-9.09Cr-1.83W, P122; Fe-10.15Cr-1.94W, T122; Fe-10.65Cr-1.87W, and 12CR; Fe-12.1Cr-1.82W in weight percent (wt. %)] [25–28]. More recently, the coarsening behavior of HPSFA has been systematically studied during long-term thermal treatment at 973 K up to 500 h, which reveals the duplex precipitates, such as, the primary and secondary, and the morphological transition of the hierarchical precipitates, which is associated with the elastic coherency of the interface between the primary precipitate and matrix [29]. However, a detailed microstructural characterization of the precipitates is necessary to elucidate the creep mechanism(s) and to achieve the further optimization of the creep properties. Critical precipitate parameters, such as the volume fraction, the composition, and the partitioning behavior of the alloying elements, should be quantified and correlated with the alloy chemistry [30,31].

Thus, the main objective of the current work is to study the microstructures of the HPSFA with a nominal composition of Fe-12.7Al-10.2Cr-9.0Ni-2.2Ti-1.9Mo-0.14Zr-0.024B (in at. %) that exhibits superior creep properties for fossil-fuel power-plant applications. The above-mentioned microstructural features will be determined, using transmission-electron microscopy (TEM) and atom-probe tomography (APT).

2. Method

A plate ingot of HPSFA with a dimension of 12.7 cm × 25.4 cm × 1.9 cm was prepared by the Sophisticated Alloys, Inc., using a vacuum-induction-melting facility. The ingot was hot-isostatically pressed (HIPed) at 1473 K and 100 MPa for 4 h. Chemical analyses were conducted on the ingot to obtain the composition. The alloy was homogenized at 1473 K for 30 min, followed by air cooling, and then aged at 973 K for 100 h. The sharp-tip needle specimens with approximate dimensions of 50–150 nm in diameter and 300–700 nm in length for APT were prepared, using lift-out methods with a FEI Nova focused ion beam (FIB) [32]. The data acquisition was performed, employing a CAMECA local electrode atom probe (LEAP) 4000XHR equipped with an energy-compensated reflectron lens. The APT runs were performed in voltage and laser modes. For the voltage-mode runs, the acquisition parameters were described as follows: 50 K, 200 kHz, 20% pulse fraction, and 0.5% detection rate. For the laser-mode runs, the acquisition parameters were as follows: 30 K, 200 kHz, 25 pJ laser energy, and a 0.5–2.0% detection rate. The TEM samples were prepared in a Zeiss Auriga 40 equipped with a dual electron and FIB. A lamella having dimensions of 12 μm × 6 μm × 1 μm was cut from a heat-treated bulk alloy sample with 30 keV Ga ions. The lamella was lifted out from the bulk sample, transferred to a Cu-grid, and thinned to a thickness of ~100 nm via FIB milling, which was, then, followed by a 5-kV final ion polish to remove the FIB-damaged surface and oxide layer. The TEM was conducted, using a Zeiss Libra 200 MC TEM at an acceleration voltage of 200 kV.

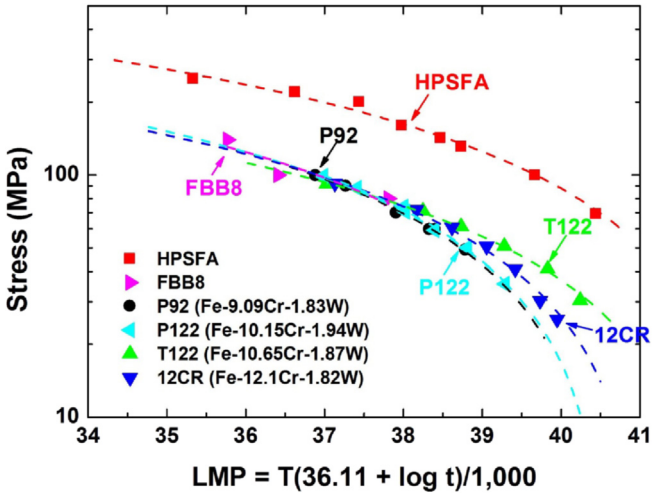

Fig. 1. Larson-Miller parameters (LMP) for HPSFA [24], FBB8 [25], and several conventional steels (P92, P122, T122, and 12CR) [26–29], where the LMP is calculated from T(36.11 + log t)/1000 (T = temperature in Kelvin, and t = time to rupture in hours).

3. Results and discussions

Fig. 2(a)-(b) show the dark-field (DF) TEM images acquired with the specimen oriented along the [110] zone axis using two different reflections in the same region of the sample aged at 973 K for 100 h. The inset in Fig. 2 shows the [110] zone-axis diffraction pattern, where two superlattice reflections were used (marked by red and white circles) to form the DF images. The <111> reflection (a red circle) is unique to the $L2_1$ structure, and, thus, the bright phases in Fig. 2(a) are the $L2_1$ phases. In contrast, when imaged using the <020> reflection (a white circle), which is a common reflection to both $L2_1$ and B2 structures, a slightly-different morphology of the primary precipitate with an average width of 90 nm [23] is observed, as shown in Fig. 2(b). By comparing two images, the B2 and $L2_1$ phases within the precipitate can be differentiated, as marked by white and red arrows, respectively. Specifically, the contrast difference within the precipitate can be observed in Fig. 2(a), which results from the presence of either an anti-phase boundary or another phase in the primary $L2_1$ precipitate, as observed in a similar Fe alloy [33]. Previously, the DF-TEM imaging was used to reveal the formation of the nano-scaled B2 zones in the primary $L2_1$-precipitates [23], and, thus, the narrow zones are likely the B2-type phases.

To verify the TEM results, APT was conducted, the results of which are shown in Fig. 3. Fig. 3(a) shows two iso-concentration surfaces, 10 at. %-Ti and 10 at. %-Ni, which clearly indicate the presence of the B2 and $L2_1$ phases in the precipitates. The compositions of the B2 and $L2_1$ phases derived from the APT analysis are $Ni_{42.8}Al_{38.2}Fe_{14.0}Ti_{4.4}Cr_{0.4}Mo_{0.1}$ and $Ni_{36.2}Al_{29.3}Fe_{18.1}Ti_{15.4}Cr_{0.6}Mo_{0.5}$ in at. %, respectively. A proximity-histogram composition profile between the B2 and $L2_1$ phases is presented in Fig. 3(b), and clearly reveals the Ni, Al, Ti, and Fe partitioning behavior within the primary precipitate. The APT results revealed the formation of secondary nm-size precipitates in the matrix, as was also observed in alloy FBB8 [19]. A 7.6 at. %-(Ni + Ti) iso-concentration surface is shown in Fig. 3(c), which clearly shows the distribution of ultra-fine secondary precipitates in the matrix. The compositions of the matrix, $L2_1$, B2, and secondary precipitates, obtained from the APT results, are summarized in Table 1. Similar duplex precipitates were observed in the NiAl-strengthened ferritic and Ni-based alloys [15,34,35]. Moreover, the microstructural evolution of the HPSFA

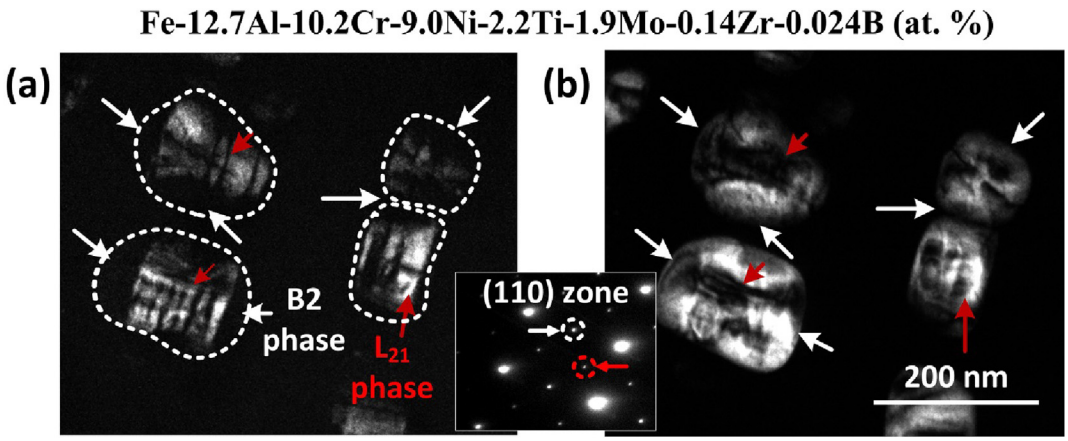

Fig. 2. Dark-field transmission-electron microscopy (DF-TEM) images acquired with the sample oriented along the [110] zone axis using (a) <111> and (b) <020> superlattice reflections with an inset of the [110] selected-area-diffraction pattern.

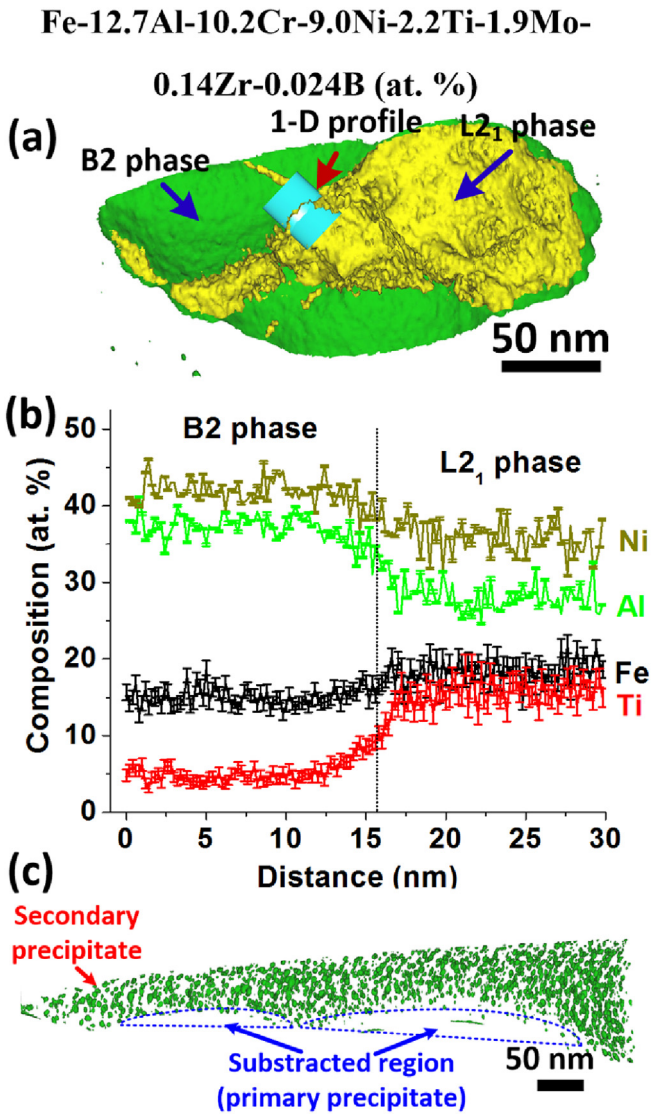

Fig. 3. Atom-probe-tomography (APT) results: (a) iso-concentration surfaces of 10 at. %-Ti (yellow) and 10 at. %-Ni (green), (b) a composition profile of the B2 and $L2_1$ phases along the one-dimensional (1-D) profile in (a), and (c) a 7.6 at. %-(Ni + Ti) iso-concentration surface (green). (For interpretation of the references to colour in this figure legend, the reader is referred to the web version of this article.)

was studied during a systematic heat-treatment at 973 K up to 500 h using TEM and APT [29], which exhibits that the size of the secondary precipitate does not vary (no coarsening). Also, similar observation was reported in a NiAl-strengthened ferritic alloy which indicates that the size of the secondary precipitates is independent on aging time at 973 K, but on aging temperatures (higher temperatures give rise to the larger secondary precipitates) [36]. Based on these observations, it is believed that the ultra-fine precipitates are formed during air cooling and completely dissolved in the matrix at 973 K [19]. Thus, these secondary precipitates significantly contribute to the room-temperature strengthening behavior, but could not influence the creep properties at 973 K. The effect of the secondary precipitates on the mechanical properties is beyond the scope of this paper, and will be investigated in the future study.

The size and volume fraction of the secondary precipitates were derived from the analysis of the APT needle specimen that only included the matrix and secondary precipitates and was performed by subtracting the primary precipitates, as shown in Fig. 3(c). The average size and volume fraction of the secondary precipitates were determined to be 2.05 ± 0.85 nm and 2.785%, respectively.

By considering the secondary precipitates in the matrix, the volume fraction of the primary precipitates can be calculated, as follows,

$$V'_m + V_{po} = 1, \quad (1)$$

where $V'_m = V_m + V_{S.P}$, $V_{S.P} = V'_m \times V'_{S.P}$, $V_{po} = V_{L21} + V_{B2}$

where V'_m is the volume fraction of the matrix, including the secondary precipitate, V_{po} is the volume fraction of the primary precipitate including $L2_1$ (V_{L21}) and B2 (V_{B2}) phases, V_m is the volume fractions of the matrix, and $V_{S.P}$ and $V'_{S.P}$ are the volume fractions of the secondary precipitates in the bulk material and in the matrix, respectively. The V_{po} can be described by the lever rule,

$$V_{po} = \frac{C_o - C_m}{C_{po} - C_m} \quad (2)$$

where C_o, C_m, and C_{po} are the compositions of the bulk sample, matrix, and primary precipitate, respectively. The C_{po} can be given by,

Table 1
Chemical compositions of phases in a Fe-12.6Al-10.1Cr-8.9Ni-2.2Ti-1.8Mo (at. %) alloy obtained, using the chemical analysis (bulk) and APT [24]. (C_o; bulk composition, C_{L21}; $L2_1$ composition, C_{B2}; B2 composition, C_m; Fe matrix composition, $C_{S.P}$; secondary precipitate composition, C'_m; combined compositions of the secondary precipitates and matrix, C_{po}; primary precipitate compositions).

Composition	Material	Phase	Al	Fe	Ni	Ti	Mo	Cr
Experimental	Bulk	(C_o)	12.518	64.243	8.977	2.157	1.834	10.134
	Primary precipitate	$L2_1$ (C_{L21})	29.253 ± 0.230	18.057 ± 0.188	36.235 ± 0.209	15.399 ± 0.188	0.466 ± 0.037	0.591 ± 0.048
		B2 (C_{B2})	38.206 ± 0.039	14.030 ± 0.028	42.826 ± 0.037	4.428 ± 0.015	0.075 ± 0.003	0.432 ± 0.005
	Matrix	Fe (C_m)	7.096 ± 0.018	75.859 ± 0.033	1.548 ± 0.009	0.407 ± 0.005	2.283 ± 0.010	12.807 ± 0.026
	Secondary precipitate	B2 ($C_{S.P}$)	34.449 ± 1.109	17.788 ± 0.939	41.580 ± 1.260	3.105 ± 0.437	0.698 ± 0.241	2.376 ± 0.372
Calculated	Combining matrix	Fe (C'_m)	7.858 ± 0.044	74.242 ± 0.036	2.663 ± 0.032	0.482 ± 0.162	2.239 ± 0.152	12.517 ± 0.044
	Primary precipitate	$L2_1$ + B2 (C_{po})	34.795 ± 0.044	16.445 ± 0.036	39.160 ± 0.032	10.163 ± 0.162	−0.101 ± 0.152	−1.255 ± 0.044

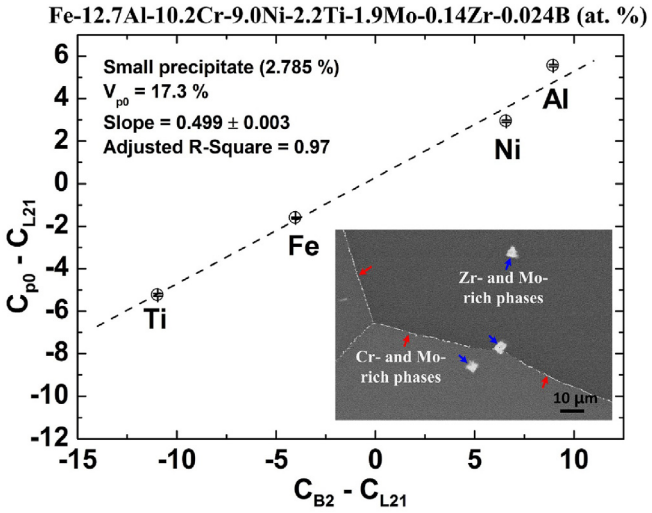

Fig. 4. A plot of (C_{po} - C_{L21}) vs. (C_{B2} - C_{L21}) used to calculate the volume fractions of B2 and $L2_1$ phases within the primary precipitate. An inset scanning-electron-microscopy (SEM) image shows Mo-, Cr-, and Zr-rich phases.

$$C_{p0} = \frac{C_0 - C'_m}{V_{p0}} + C'_m \quad \text{where } C'_m = V'_{S.P} \times (C_{S.P} - C_m) + C_m \tag{3}$$

where C'_m and $C_{S.P}$ are the combined compositions of the secondary precipitates and matrix, and the secondary precipitates, respectively. C_{po} and, thus, V_{po} cannot be determined from the APT results, since the primary precipitate contains the B2 and $L2_1$ phases with unknown volume fractions. Thus, in order to derive C_{po} and V_{po}, a similar equation was adopted, defined as,

$$\frac{V_{B2}}{V_{L21}} = \frac{C_{po} - C_{L21}}{C_{B2} - C_{L21}} \tag{4}$$

where C_{L21} and C_{B2} are the compositions of the $L2_1$ and B2 phases, respectively. In order to acquire C_{po}, V_{B2}, and V_{po}, and, thus, V_m and V_{L21}, reasonable values of V_{po} ranging from 15.0 to 20.0%, which bracket the value (16.3%) determined from the SEM-image analysis [23], the volume fraction of the primary precipitates of $V_{po} = 17.3\%$ from the best linear fit of a plot of (C_{po} - C_{L21}) vs. (C_{B2} - C_{L21}) in Fig. 4 can be achieved, and V_{B2} accounts for 49.9% of V_{po}. The calculated compositions of C'_m and C_{po} are also summarized in Table 1. It should be noted that the calculated C_{po} of Cr and Mo has negative values in Table 1, which could result from the formation of additional minor phases. Indeed, minor phases are often observed within grains and along grain boundaries, as shown in the inset of Fig. 4. The scanning-electron-microscopy (SEM) energy-dispersive X-ray analysis indicates that these minor phases are enriched in Zr, Cr, and Mo, which could affect the current calculation. Therefore, four elements (Fe, Al, Ni, and Ti), which constitute the primary matrix and precipitate phases, were used for the current plots. From these data, values of volume fractions of the phases in the system were deduced: $V_m = 80.4\%$, $V_{S.P} = 2.3\%$, $V_{B2} = 8.6\%$, and $V_{L21} = 8.7\%$. Note that $V'_{S.P}$ (2.785%) was derived from the volume of the APT-needle specimen only containing the matrix and secondary precipitates [Fig. 3(c)]. Thus, the overall fraction of the secondary precipitate in the bulk material ($V_{S.P}$) was derived, using Equation (1), and is 2.3%. The volume fraction of the primary precipitates ($V_{po} = 17.3\%$) derived from the APT-composition analysis is in good agreement with that determined by the SEM-imaging analysis (16.3%) [23].

4. Conclusions

The aged microstructure of a hierarchical-precipitate-strengthened ferritic alloy has been characterized, using TEM and APT. HPSFA consists of duplex precipitates embedded in the Fe matrix; primary precipitates with an average width of 90 nm, and secondary precipitates with an average radius of 2 nm. The primary precipitate contains a mixture of the B2-type NiAl and $L2_1$-type Ni_2TiAl phases. The compositions of the B2 and $L2_1$ phases are $Ni_{42.8}Al_{38.2}Fe_{14.0}Ti_{4.4}Cr_{0.4}Mo_{0.1}$ and $Ni_{36.2}Al_{29.3}Fe_{18.1}Ti_{15.4}Cr_{0.6}Mo_{0.5}$ in at. %, respectively, while that of the Fe matrix is $Fe_{75.8}Cr_{12.8}Al_{7.1}Ti_{0.4}Ni_{1.5}Mo_{2.3}$ in at. %. The composition of the secondary precipitates is measured to be $Ni_{41.6}Al_{34.4}Fe_{17.8}Ti_{3.1}Cr_{2.3}Mo_{0.7}$ in at. %, which is close to that of the B2 phase in the primary precipitate. Based on the APT-composition analysis, the volume fractions of the matrix, secondary precipitate, $L2_1$ and B2 phases in the primary precipitate are derived, using the lever rule, and are 80.4, 2.3, 8.7, and 8.6%, respectively.

Acknowledgements

The present research is supported by the Department of Energy (DOE), Office of Fossil Energy Program, under Grants of DE-09NT0008089, DE-FE0005868, DE-FE-0011194, and DE-FE-0024054 with Mr. Richard Dunst, Mr. Vito Cedro, Dr. Patricia Rawls, Mr. Steven Markovich, and Dr. Jessica Mullen as the program managers. The research was supported as part of a user proposal through ORNL's Center for Nanophase Materials Sciences (CNMS), which is a DOE Office of Science User Facility.

References

[1] R. Viswanathan, W. Bakker, Materials for ultrasupercritical coal power plants—Boiler materials: Part 1, J. Mater. Eng. Perform. 10 (2001) 81–95.
[2] R. Viswanathan, W. Bakker, Materials for ultrasupercritical coal power plants—Turbine materials: Part II, J. Mater. Eng. Perform. 10 (2001) 96–101.
[3] S.H. Kim, H. Kim, N.J. Kim, Brittle intermetallic compound makes ultrastrong low-density steel with large ductility, Nature 518 (2015) 77–79.

[4] Y. Yamamoto, M.P. Brady, Z.P. Lu, P.J. Maziasz, C.T. Liu, B.A. Pint, K.L. More, H. Meyer, E.A. Payzant, Creep-Resistant, Al_2O_3-forming austenitic stainless steels, Science 316 (2007) 433–436.
[5] R. Kaybyshev, V. Skorobogatykh, I. Shchenkova, New martensitic steels for fossil power plant: creep resistance, Phys. Met. Metallogr. 109 (2010) 186–200.
[6] M. Taneike, F. Abe, K. Sawada, Creep-strengthening of steel at high temperatures using nano-sized carbonitride dispersions, Nature 424 (2003) 294–296.
[7] P.J. Ennis, A. Czyrska-Filemonowicz, Recent advances in creep-resistant steels for power plant applications, Sadhana 28 (2003) 709–730.
[8] F. Abe, S. Nakazawa, H. Araki, T. Noda, The role of microstructural instability on creep behavior of a martensitic 9Cr-2W steel, Metall. Trans. A 23 (1992) 469–477.
[9] G. Eggeler, The effect of long-term creep on particle coarsening in tempered martensite ferritic steels, Acta Metall. 37 (1989) 3225–3234.
[10] F. Masuyama, J.P. Shingledecker, Recent status of ASME code on creep strength enhanced ferritic steels, Proc. Eng. 55 (2013) 314–325.
[11] L.L. Hsiung, M.J. Fluss, S.J. Tumey, B.W. Choi, Y. Serruys, F. Willaime, A. Kimura, Formation mechanism and the role of nanoparticles in Fe-Cr ODS steels developed for radiation tolerance, Phys. Rev. B 82 (2010) 184103.
[12] Y. Jiang, J.R. Smith, G.R. Odette, Formation of Y-Ti-O nanoclusters in nanostructured ferritic alloys: a first-principles study, Phys. Rev. B 79 (2009) 064103.
[13] R. Viswanathan, K. Coleman, U. Rao, Materials for ultra-supercritical coal-fired power plant boilers, Int. J. Pres. Ves. Pip. 83 (2006) 778–783.
[14] S.M. Zhu, S.C. Tjong, J.K.L. Lai, Creep behavior of a β′(NiAl) precipitation strengthened ferritic Fe–Cr–Ni–Al alloy, Acta Mater. 46 (1998) 2969–2976.
[15] C. Stallybrass, A. Schneider, G. Sauthoff, The strengthening effect of (Ni,Fe)Al precipitates on the mechanical properties at high temperatures of ferritic Fe–Al–Ni–Cr alloys, Intermetallics 13 (2005) 1263–1268.
[16] Z. Sun, C.H. Liebscher, S. Huang, Z. Teng, G. Song, G. Wang, M. Asta, M. Rawlings, M.E. Fine, P.K. Liaw, New design aspects of creep-resistant NiAl-strengthened ferritic alloys, Scr. Mater. 68 (2013) 384–388.
[17] H. Calderon, M.E. Fine, Coarsening kinetics of coherent NiAl-type precipitates in Fe-Ni-Al and Fe-Ni-Al-Mo alloys, Mater. Sci. Eng. 63 (1984) 197–208.
[18] H. Calderon, M. Fine, J. Weertman, Coarsening and morphology of β′ particles in Fe-Ni-Al-Mo ferritic alloys, Metall. Mater. Trans. A 19 (1988) 1135–1146.
[19] Z.K. Teng, M.K. Miller, G. Ghosh, C.T. Liu, S. Huang, K.F. Russell, M.E. Fine, P.K. Liaw, Characterization of nanoscale NiAl-type precipitates in a ferritic steel by electron microscopy and atom probe tomography, Scr. Mater. 63 (2010) 61–64.
[20] S. Huang, D. Brown, B. Clausen, Z. Teng, Y. Gao, P.K. Liaw, In situ neutron-diffraction studies on the creep behavior of a ferritic superalloy, Metall. Mater. Trans. A 43 (2011) 1497–1508.
[21] Z.K. Teng, G. Ghosh, M.K. Miller, S. Huang, B. Clausen, D.W. Brown, P.K. Liaw, Neutron-diffraction study and modeling of the lattice parameters of a NiAl-precipitate-strengthened Fe-based alloy, Acta Mater. 60 (2012) 5362–5369.
[22] S. Huang, Y. Gao, K. An, L. Zheng, W. Wu, Z. Teng, P.K. Liaw, Deformation mechanisms in a precipitation-strengthened ferritic superalloy revealed by in situ neutron diffraction studies at elevated temperatures, Acta Mater. 83 (2015) 137–148.
[23] G. Song, Z. Sun, L. Li, X. Xu, M. Rawlings, C.H. Liebscher, B. Clausen, J. Poplawsky, D.N. Leonard, S. Huang, Z. Teng, C.T. Liu, M.D. Asta, Y. Gao, D.C. Dunand, G. Ghosh, M. Chen, M.E. Fine, P.K. Liaw, Ferritic alloy with extreme creep resistance via coherent hierarchical precipitates, Sci. Rep. 5 (2015) 16327.
[24] N.Q. Vo, C.H. Liebscher, M.J. Rawlings, M. Asta, D.C. Dunand, Creep properties and microstructure of a precipitation-strengthened ferritic Fe–Al–Ni–Cr alloy, Acta Mater. 71 (2014) 89–99.
[25] M. Yoshizawa, M. Igarashi, K. Moriguchi, A. Iseda, H.G. Armaki, K. Maruyama, Effect of precipitates on long-term creep deformation properties of P92 and P122 type advanced ferritic steels for USC power plants, Mater. Sci. Eng. A 510–511 (2009) 162–168.
[26] K. Sawada, K. Kubo, F. Abe, Creep behavior and stability of MX precipitates at high temperature in 9Cr–0.5Mo–1.8W–VNb steel, Mater. Sci. Eng. A 319–321 (2001) 784–787.
[27] F. Masuyama, N. Komai, Evaluation of long-term creep rupture strength of tungsten-strengthened advanced 9-12% Cr steels, Key Eng. Mater 171 (2000) 179–188.
[28] K. Kimura, K. Sawada, H. Kushima, Y. Toda, Long-term creep strength of creep strength enhanced ferritic steels, in: K. Cen, Y. Chi, F. Wang (Eds.), Challenges of Power Engineering and Environment, Springer Berlin Heidelberg, 2007, pp. 1059–1065.
[29] G. Song, Z. Sun, J.D. Poplawsky, Y. Gao, P.K. Liaw, Microstructural evolution of single Ni_2TiAl or hierarchical NiAl/Ni_2TiAl precipitates in Fe-Ni-Al-Cr-Ti ferritic alloys during thermal treatment for elevated-temperature applications, Acta Mater. 127 (2017) 1–16, http://dx.doi.org/10.1016/j.actamat.2017.01.011.
[30] Z.W. Zhang, C.T. Liu, X.L. Wang, K.C. Littrell, M.K. Miller, K. An, B.A. Chin, From embryos to precipitates: a study of nucleation and growth in a multicomponent ferritic steel, Phys. Rev. B 84 (2011) 174114.
[31] R. Srinivasan, R. Banerjee, J.Y. Hwang, G.B. Viswanathan, J. Tiley, D.M. Dimiduk, H.L. Fraser, Atomic scale structure and chemical composition across order-disorder interfaces, Phys. Rev. Lett. 102 (2009) 086101.
[32] D.J. Larson, T.J. Prosa, R.M. Ulfig, B.P. Geiser, T.F. Kelly, Local Electrode Atom Probe Tomography, Springer, New York, 2013.
[33] C.H. Liebscher, V. Radmilovic, U. Dahmen, M. Asta, G. Ghosh, On the formation of hierarchically structured $L2_1$-Ni_2TiAl type precipitates in a ferritic alloy, J. Mater. Sci. 48 (2013) 2067–2075.
[34] K. Kakehi, Effect of primary and secondary precipitates on creep strength of Ni-base superalloy single crystals, Mater. Sci. Eng. A 278 (2000) 135–141.
[35] Z. Sun, G. Song, J. Ilavsky, P.K. Liaw, Duplex precipitates and their effects on the room-temperature fracture behaviour of a NiAl-strengthened ferritic alloy, Mater. Res. Lett. 3 (2015) 128–134.
[36] Z. Sun, G. Song, J. Ilavsky, G. Ghosh, P.K. Liaw, Nano-sized precipitate stability and its controlling factors in a NiAl-strengthened ferritic alloy, Sci. Rep. 5 (2015) 16081.